SOURCE AIR FEEDING CONVECTION WITHIN A NOCTURNAL MESOSCALE CONVECTIVE SYSTEM DURING THE EVOLUTION FROM SURFACE-BASED TO ELEVATED CONVECTION

BY

JESSICA JOY CHOATE

THESIS

Submitted in partial fulfillment of the requirements
for the degree of Master of Science in Atmospheric Sciences
in the Graduate College of the
University of Illinois at Urbana-Champaign, 2016

Urbana, Illinois

Master's Committee:

Professor Robert M. Rauber
Professor Greg M. McFarquhar
Research Scientist Brian F. Jewett

Abstract

Although nocturnal convection is frequently observed, the mechanisms that allow nocturnal mesoscale convective systems (MCSs) to persist are still not well understood. On 9 August 2014 at approximately 2000 UTC, a regime of upslope flow owing to a weak shortwave impulse in the lee of the Rocky Mountains spawned a convective complex near the Colorado-Kansas border. Following storm initiation, the system grew upscale into a southeastward-propagating MCS, which became elevated as it continued into the overnight hours, producing severe surface winds and severe hail.

This study investigates the elevation above ground level (AGL) from which air parcels with the greatest convective available potential energy (CAPE) originate and support the development and maintenance of elevated convection. The analysis of this system uses WSR-88D composite reflectivity data, a short term forecast from the Weather Research and Forecasting (WRF) model, and back trajectories produced by the Hybrid Single-Particle Lagrangian Integrated Trajectory (HYSPLIT) model. This paper describes the evolution of the boundary layer as well as the spatial and temporal progression of the altitude of the most unstable (MU) CAPE of air parcels associated with the elevated convection and the connection the source air had with the highest reflectivity produced in the MCS. The change in the source of these parcels over time shows that this particular MCS became elevated and sustained itself off parcels with MU CAPE residing between 1.0 and 1.5 km. It was found that these parcels originated in a different air mass than the parcels with MU CAPE feeding the storm from the surface earlier in the system's evolution.

Acknowledgments

I would like to thank my advisors, Prof. Bob Rauber, Prof. Greg McFarquhar, and Dr. Brian Jewett for their constant guidance and support throughout my research at the University of Illinois Urbana-Champaign. They gave me the push to reach the potential I didn't always see in myself.

This project could not have been completed without help troubleshooting many research and programming issues from Dr. Stephen Nesbitt, Daniel Stechman, and Bethany Fay and many other members of the UIUC Department of Atmospheric Sciences. I would also like to thank all the professors of the UIUC DAS for providing me with an excellent education and igniting my curiosity for further atmospheric research.

My support system outside of work has been just as influential on the success of my degree as my support within the department. There are a countless number of people who have encouraged me along the way but I would like to specifically thank Emily Hogan, Kellie Kroscher, Nicole Larsen, Anthony Lupo, Daniel Stechman, and Zachary Wienhoff for their immense impact on the completion of this research.

Absolutely none of what I have accomplished at UIUC or elsewhere could have happened without the continued love and support of my parents Scott and Karen Choate. Thank you so much for everything you do and I love you.

I would like to thank the University of Illinois Urbana-Champaign for several teaching and research assistantships so I was able to continue my education and research at the university. Lastly, I would like to thank the National Science Foundation for funding under grant AGS-1359098.

Table of Contents

Chapter 1. Introduction……..1

Chapter 2. Data and Methodology……5

Chapter 3. 9 and 10 August 2014 Storm System……7

Chapter 4. WRF Reflectivity Evolution……8

Chapter 5. Results……10

Chapter 6. Summary and Conclusions……18

Table……21

Figures……22

References……37

Chapter 1

Introduction

Mesoscale convective systems (MCSs) are one of Earth's most prevalent rain producers (Houze 2004; Schumacher and Johnson 2006; Stevenson and Schumacher 2014). In the United States, they are responsible for more than half of the extreme rainfall events during the summer months (Fritsch et al. 1986; Schumacher and Johnson 2005). Extreme rain events are frequently observed over the southern plains due to their proximity to the lee of the Rocky Mountains (Bradley and Smith 1994). While much of the Earth's most intense rain-producing convective systems are based at the sun-heated surface during the day, many MCSs also occur at night when solar radiation is no longer a viable energy source (Colman 1990a,b; Moore et al. 2003). Such nocturnal systems are often considered elevated, since the surface becomes stable overnight, and the storms must feed off energy which originates aloft (Trier et al. 2006; Bryan and Weisman 2006). While surface-based MCSs are often indistinguishable on radar from their elevated counterparts, the most common severe hazards, and overall intensity of the storms, can vary greatly depending on where the storm receives it energy, making hazardous weather forecasting for these events difficult (Schmidt and Cotton 1986; Moore et al. 2003; Atkins and Cunningham 2006; Bryan and Weisman 2006).

While there are many reasons proposed to explain how MCSs evolve over a diurnal cycle, most can be attributed to either thermodynamic processes, focusing on the static stability of the system, or dynamical processes, focusing on mass convergence into the convective complex (Wallace 1975). Moisture is arguably the most important state variable within the environment of a long–lived system as dry-air entrained into systems can

reduce the buoyancy of convective plumes by enhancing evaporative cooling (Wu et al. 2009). Thermodynamic processes such as radiative cooling from cloud top and low-level warm advection of moist air have been proposed as mechanisms enchancing nocturnal convection over the central United States. The low-level jet can provide an elevated source of unstable air for systems to sustain themselves once the surface becomes stabilized after sunset and sustained convergence can occur along the jet's leading edge. Most work on this topic has investigated long-lived systems in the presence of a low-level jet. Additional research on systems in the absence of a jet could help quantify the importance of the jet in nocturnal systems (Wallace 1975; French and Parker 2010).

The American Meteorological Society (2016) defines elevated convection as "convection that originates from an atmospheric layer above the boundary layer." Moore et al. (2003) researched elevated systems and evaluated convective available potential energy (CAPE), particularly in the vicinity of frontal boundaries. They found that elevated MCSs typically are located to the north of an east-west surface front over the cold sector and towards the leading edge of low-level jet in elevated environments. Further, Horgan et al. (2007) found that all of the elevated severe cases they analyzed were associated with elevated CAPE, weak surface easteries, and shallow surface stable layers. Trier et al. (2014) simulated several convective systems and showed that the "vertical structure of the mesoscale environment plays a key role in the evolution and sustenance of convection long after convection initiation and internal MCS circulations develop, particularly in elevated systems." Although many previous studies have also examined MCSs, most have focused on their impacts rather than their development and transition from surface-based to long-lived elevated systems (e.g., Kincer 1916; Rochette and Moore 1996; Moore et al. 2003;

Weisman 1993; Schumacher and Johnson 2006; Trapp et al. 2005; Bryan 2005; Wakimoto et al. 2006; Horgan et al. 2007; Billings and Parker 2012; French and Parker 2010; Du and Rotunno 2014; Erlingis and Barros 2014; Schumacher 2015).

The characteristics of the air mass feeding into a system affect its lifetime. For example, a dry airmass can enhance evaporative cooling, leading to more intense downdrafts and systems dominated by outflow. A stronger cold pool, which can serve as an enhanced source of lift, can in turn become too strong such that it spreads too far ahead of the convection so that new convective cells are not triggered along the line (James and Markowski 2010). Because dry air can also be entrained into updrafts, James and Markowski (2010) showed that dry air aloft can weaken systems, reducing the total condensation and rainfall within quasi-linear convective systems. These effects were enhanced in low CAPE environments.

CAPE is a fundamental parameter that determines the likelihood of convection and its intensity (Doswell and Rasmussen 1994). Since CAPE is a vertically integrated quantity, the potential energy available for lifting parcels from different levels of the atmosphere can be determined by changing the level from which the integration is initiated. McCaul and Weisman (1996) and Blanchard (1998) showed that separating CAPE into multiple layers can provide insight into the development and evolution of convective systems since the distribution of CAPE, and the location of the layer with the largest CAPE, can strongly impact the maximum vertical velocities achieved.

This study analyzes characteristics of the pre-storm environment of MCS convection that transitions from surface-based to elevated during the evening hours on 9 and 10 August 2014. For the entirety of this study, “pre-storm” environment refers to the region

ahead of the convective system, which provides source air to the storm. Data from the WSR-88D (Weather Surveillance Radar-1988 Doppler) network, Hybrid Single-Particle Lagrangian Integrated Trajectory model (HYSPLIT), and a simulation of the Weather Research and Forecasting Model (WRF) are combined to determine where source air feeding elevated convection originated 24 hours earlier for this MCS. In particular, the trajectories are used to determine where the air arriving at the level with the most unstable parcels resided 24 hours before the MCS convection was active. Through this analysis, the evolution of source air in relation to the distribution of CAPE during the transition from a surface-based convective system to an elevated convective system can be better understood. This storm was analyzed because it transitioned from a surface-based system to an elevated system in the absence of a distinct low-level jet.

Chapter 2

Data and Methodology

WSR 88D radar reflectivity factor (hereafter, reflectivity) data from sites within range of the 9 and 10 August 2014 MCS were composited to produce reflectivity images. The lowest four sweeps of reflectivity data were included to characterize the shape, location, intensity, and evolution of the MCS every 5 minutes starting at the time of initiation, 2000 UTC, 9 August. Radar locations at any given time were chosen based on proximity to the convection. Four or five sites were used in a composite. The center of the domain around the MCS shifted eastward as the storm evolved, while the size of the analysis domain remained constant. Domain centers, radar locations, and times for each domain shift are given in Table 1.

A WRF Model (version 3.5.1) simulation was used in conjunction with the observed reflectivity to provide information on the MCS's thermodynamic environment. The simulation was initialized with the 3-h North American Mesoscale Model (NAM) centered at 38.5N and 98W with 9-km grid spacing and 60 vertical levels. Thompson microphysics (Thompson et al. 2008) and Rapid Radiative Transfer Model for Global Climate Models (RRTMG, Iacono et al. 2008) shortwave/longwave radiation were used. Convection was parameterized using the Betts-Miller-Janjic parameterization (Janjic 1994). The simulation was initialized on 0000 UTC 9 August 2014 and was used to analyze the pre-storm environmental CAPE distribution for parcels originating at the surface, 0.5 km, 1.0 km, 1.5 km, and 2.0 km.

Sources of the pre-storm environmental air feeding into the convective system were determined by computing back-trajectories of air parcels along and ahead of the convective

line using the HYSPLIT model (Stein et al. 2015). The HYSPLIT model was initially designed and used to determine the transport of dust, aerosols, or gaseous toxins and chemicals (e.g., Han et al. 2005; McGowan and Clark 2008; Dreher 2009; Alam et al. 2011; Yerramilli et al. 2012). More recent studies have used it to investigate larger storm environments and the origin of air parcels (e.g., Dreher 2009; Rauber et al. 2014, 2015, Stein et al. 2015). Archived data from NAM 12-km runs were used to initialize the HYSPLIT model. Backward 24-hr trajectories were calculated every hour at locations along and ahead of the convective line. Trajectories were computed every hour from 2000 UTC 9 August 2014 to 0600 UTC 10 August 2014 for parcels originating at the surface and aloft at 500 m, 1.0 km, 1.5 km , and 2.0 km.

Chapter 3

9 and 10 August 2014 Storm System

On 9 August 2014 at approximately 2100 UTC, upslope flow associated with a weak shortwave at 700 mb passing to the lee of the Rocky Mountains spawned a convective complex in eastern Colorado. A weak north-south oriented dryline extended southward from a low in west-central Nebraska with a stationary front aligned from central South Dakota through Oklahoma (Figure 1). Figure 2 shows storm evolution every three hours from 2100 UTC through 0600 UTC, the time period that is the focus of this study. Following storm initiation, the system grew upscale into a southeastward-propagating MCS, which became elevated as it continued into the overnight hours. A gust front appeared as a fine line in the WSR-88D reflectivity field at roughly 0130 UTC on 10 August and persisted for several hours (Figure 2). The disorganized northern convection began to merge with the main convective line about 0400 UTC, increasing the size and further expanding the MCS. A strong convective line persisted through sunrise on 10 August. Over its lifetime, the MCS produced a defined and persistent outflow boundary, with severe conditions such as severe hail reaching 2.75 inches and wind gusts of 80 miles per hour after 0100 UTC.

Chapter 4

WRF Reflectivity Evolution

The WRF simulation is used herein for thermodynamic analysis in the environment ahead of the convective line since there was insufficient data available from standard National Weather Service soundings. Thus, it was necessary that the simulated reflectivity evolve in a spatially and temporally comparable way to the observed system such that the simulated analysis had the correct context with the observations. Figure 3 provides a comparison between the reflectivity field from the WSR-88D network and the reflectivity from WRF for four times starting shortly after initiation through several hours after sunset.

Figure 3a shows the WRF reflectivity shortly after initiation at 2100 UTC. Simulated reflectivities were weaker than the observed reflectivities, which are contoured in black in Figure 3. The center of western cell in the simulation was displaced to the northwest by about 65 km while the eastern cell was positioned between two observed clusters with the highest reflectivity to the south of the northeast cell by approximately 25 km. The shape of the WRF reflectivity field was smoother than the observed data, which is expected given the coarser resolution of the WRF simulation compared to that of the radar data. Three hours later, and roughly an hour and a half before sunset (0000 UTC; Fig. 3b), the WRF-simulated MCS organized and grew upscale more rapidly than the observed storm and moved faster to the east and north. The western convection was displaced too far to the west but had the same "notched" shape. Maximum reflectivities in the simulation were within approximately within 5 dBZ of those observed, with the convective area larger in the simulation. The simulated storm already began to develop a stratiform region by 0000 UTC. Sunset occurred at 0139 UTC. Figure 3c depicts the system 81 minutes after sunset

(0300 UTC). The simulation reproduced the bowing shape of the main convective line. The simulated convective line was displaced to the east relative to the observations by roughly 35 km. The northern ends of both the simulated and observed systems were less organized, with the WRF reflectivity again smoother than the observed data. Maximum reflectivities along the simulated convective line remain within approximately 5 dBZ of the observed values. Figure 3d shows the line 4 hours and 21 minutes after sunset (0600 UTC). At this time, the model reflectivity has a more defined northern convective line with a continued bowing shape while the observed system has a more linear leading edge, which was less well defined. The simulation had a wider stratiform region on its southern end, about 85 km larger than the observed stratiform region. The simulation is used only for analysis of the environment ahead of the convective line. The fact that the simulated reflectivity evolved analogously or slightly to the east of the observed system lends confidence that the model environment ahead of the system is representative of the pre-storm environment and can be used to understand characteristics of the pre-storm environment and its evolution through the evening. In the following section, 24 hr air parcel trajectories are calculated at locations along and ahead of the convective line. First, the environment is examined to determine how the simulated mixed-layer and the distribution of CAPE evolved during the transition from daytime to night.

Chapter 5

Results

a) Thermodynamic Analysis

WRF soundings were calculated at seven locations along the convective line at 0000 UTC, 0300 UTC, and 0600 UTC. The analysis herein will focus on these times, which depict three stages of evolution: the surface-based storm, the transition period, and the elevated system. Figure 4 shows the lowest 4.0 km of the atmosphere at each of the seven points depicted in Figure 4a at 0000 UTC. Figures 4(b-h) show a conditionally unstable pre-storm environment with a well defined mixed-layer and wind shift at approximately 2.0 km, depicting the surface-based storm environment.

Figure 5 shows the pre-storm environment at 0300 UTC. The storm has grown upscale (Fig. 5a) and the mixed-layer depth has shrunk from 0000 UTC (Figs. 5(b-h)) with a stabilizing inversion developing in several locations (Figs. 5(b,c, and d), Figure 5(b-h) also has a defined wind shift, similar to what is seen at 0000 UTC, but the majority of locations see this shift at a slightly lower level, now between 1.0 km and 2.0 km, reflecting the decreasing depth of the mixed layer. These sounding show the beginning of the stabilization of the environment and the transition to elevated convection as the surface begins to lose potential to sustain convection.

Figures 6(b-h) shows a stable surfaced based inversion, of various strength, at all locations suggesting the completion of a transition to elevated convection. Of note, the wind shift in figure 6(b-h) occurs at lower altitudes between 1.0 km and 1.5 km as the mixed layer continues to weaken. Figures 4-6 do not show evidence of a low-level jet during the transition to elevated convection. Only weak southerly flow of 5-10 kts, not

characteristic of a strong jet, was present just east of the convective line.

b) CAPE Distribution

WRF simulated CAPE was calculated for parcels originating at the surface, 500 m, 1.0 km, 1.5 km, and 2.0 km. Herein, the term "near surface layer" will be used to describe the environment in the lowest levels of the surface and 500 m. Figure 7 shows the distribution of CAPE spatially, temporally, and vertically across the MCS at 0000 UTC, 0300 UTC, and 0600 UTC. From this figure, the CAPE distribution along and east of the convective line, through the lowest two kilometers of the atmosphere, and how the distribution evolves with time can be analyzed. Figure 7a shows the CAPE distribution at 0000 UTC. At this point, it is known from the soundings that there is a well-defined mixed layer extending to near 2.0 km and that the convection is surface-based (Fig. 4). This is consistent with the distribution of CAPE along the convective line in figure 7a, where the soundings were plotted. There is little visual difference in CAPE values through the lowest 2.0 km along the convective line. As distance increased to the east of the line, there are larger differences in the CAPE field between levels as CAPE approaches zero at 1.5 km and 2.0 km.

Figure 7b shows the CAPE distribution at 0300 UTC. At this time, most points along the convective line have begun to stabilize at the surface (Fig. 5). CAPE has noticeably decreased from figure 7a at all five levels. Larger values (depicted by yellow colors) than the surrounding areas along the line are seen near the southern bowing segment. These correspond with figures 5(e-g), which show the surface remaining unstable at this time compared to the other soundings further north in figure 5 which have begun to stabilize at

the surface. Although the surface is unstable along the southern bow, the largest CAPE (seen in the lime green area) occurs at 1.0 km, suggesting the transition to elevated convection had begun. The wind shift (occurring between 1.0 and 2.0 km) seen in figures 5(e-g) corresponds to this level of higher CAPE. The northern half of the MCS had CAPE values approach zero to the east at all five levels. The opposite is seen to the south. South of the bow, values along the line are near zero but increase to the east of the line. This makes it appear as if there is a northwest-southeast oriented area of locally higher CAPE starting from approximately 40N,98W to 37N,95W (Fig. 7b). This will be examined closer in the next section.

CAPE at 0600 UTC decreased from previous times (figure 7c). The surface stabilized at all points along the convective line (Fig. 6) with CAPE in the surface layers less than 1000 J kg^{-1} anywhere along the line (purples, Fig. 7c). Locally increased values (yellows) are seen at 1.0 and 1.5 km, showing the most unstable environment is located above the surface. This is also where the wind shift occurs in figure 6 between 1.0 and 1.5 km. Moving further east from the line, a northwest-southeast oriented line of locally higher CAPE is seen (Fig. 7c), similar to what was discussed in figure 7b.

Figure 8 shows the points where WRF CAPE values were calculated at the same three times as figure 7 and at 7 latitudes along the MCS. Longitudes where the CAPE calculations were performed changed with the evolving system but latitudes stayed consistent for all times. Each latitude coincides with data in panels in Figs. 9- 11.

Figure 9 shows the maximum CAPE at all levels was closest to the convective line, as seen in figure 7. The highest values of CAPE were the surface-based CAPE (below 500 m) with values decreasing as height AGL increases. Surface-based CAPE along the

northernmost section (Fig. 9a) reached 1500 J kg^{-1}, while surface-based CAPE along the rest of the convective line was between 2500 and 3500 J kg^{-1}. This is consistent with figure 4a, which has the shallowest mixed layer. There is a significant drop in CAPE following the maximum values in all panels. But, moving approximately two to three longitudinal points (~222-333 km) away from the convective line (dashed gray lines) in each panel, there is another slight increase in CAPE in all latitudinal panels (Fig. 9).

The distribution of CAPE at 0300 UTC (10 PM CDT) suggests the transition from surface-based to elevated convection had mostly occurred (Fig. 7b). The CAPE is maximized at 1.0 km AGL along the storm's bowing segment, in excess of 2000 J kg^{-1} (Figs. 10e,f), corresponding to the locally enhanced values seen in figure 7b. Figures 10c and d show 1.5 km and 2.0 km AGL levels having the largest CAPE in those latitudes with 1.5 km CAPE exceeding the surface-based CAPE by approximately 700 J kg^{-1} (Fig. 10d). CAPE to the east of these maxima decreases, similar to what is seen at 0000 UTC (Fig. 9). Unlike figure 9, a secondary increase in CAPE (to the east of the convective line where maximum CAPE is location) is less defined, but still noticeable approximately two longitudinal points (~222 km) ahead of the maxima in each panel, particularly in figures 10(c-f). This agrees with the "northwest-southeast oriented area of locally higher CAPE" discussed in figure 7b.

CAPE continued to decrease at all levels by 0600 UTC (1 AM CDT), as seen in figure 7c. Figures 11a-e show all CAPE values had decreases to below 750 J kg^{-1} at all points along and north of 39 degrees latitude. Just to the south, at 38N, CAPE spikes to 1750 J kg^{-1} at 1.0 km and 1.5 km, exceeding surface-based CAPE by approximately 1000 J kg^{-1} (Fig. 11f), matching the local maxima seen in figure 7c at those levels. Figure 11g shows the largest differences in CAPE among levels by approximately 1700 J kg^{-1}, with the highest

values at 1.0 km. This suggests the energy for convection at this point in storm evolution was being provided between 1.0 km and 1.5 km, implying the system is elevated. The distribution of CAPE is consistent with the completion of the transition from surface-based to elevated convection seen in figures 4-6.

c) Air Parcel Trajectories

Back trajectories were run for 24 hours using HYSPLIT to determine where parcels feeding the MCS convective line originated and the path they took during the evolution from surface-based to elevated convection. Figure 12(a-e) shows the trajectory parcels took ending at 0000 UTC. It is important to note that the trajectories represent travel over 24 hours while the reflectivity represents a static image of the MCS at one point in time. The trajectories coming from the west are not traveling over the storm system, but rather are moving towards the east ahead of the storm system. When referencing the location of parcel initiation 24 hours prior it should be understood that this direction is relative to the ending location of the parcels being discussed. All ending locations are marked with a symbol ahead of the convective line. All parcels ending at the surface and 500m at 0000 UTC (Figures 12a and 12b) originated from the east or southeast of their ending location (IN, IL, IA, MO, KS, and OK). At this time, the surface is conditionally unstable, as seen in the soundings (Fig. 4), and surface parcels had the largest CAPE (Fig. 9). The majority of trajectories ending at levels higher AGL at 0000 UTC originated from the west and southwest (CO, NM, and TX) at 1.0 and 1.5 km (Fig. 12c-d), instead of the east, as at the surface and 500 m (Fig. 12a-b). The 1.0 and 1.5 km northernmost parcels were the only ones still originating from the east (IL and IN), where soundings show there is the

shallowest mixed layer compared to other locations (Fig. 4b) and the lowest CAPE (Fig. 9a). The largest shift in origination of parcel trajectories, from the other levels AGL, is seen at 2.0 km (Fig. 12e), which is consistent with the location of the wind shift seen in figure 4. The majority of parcels at this level originated in NM, CO, and WY.

At 0300 UTC, parcels ending at the surface and 500 m originated from the east and southeast (Fig. 13a-b), similar to what was seen at 0000 UTC (Fig. 12a-b). For trajectories ending at higher levels AGL at 0300 UTC, parcels took a path from the southwest of their ending location, originating in NE, CO, NM, and TX (Fig. 13c-e), similar to 0000 UTC (Fig. 12c-e). Comparing the parcel trajectories at 1.0, 1.5, and 2.0 km (panels c, d, and e, respectively) at 0000 UTC and 0300 UTC (Figs. 12 and 13), more parcels origniated to the west-southwest of their ending locations at 0300 UTC than at 0000 UTC. The few trajectories traveling from the east at 0300 UTC ended at locations futher away from the convective line than the trajectories arriving from the east at 0000 UTC. Although parcels traveling from the east at 0300 UTC ended further away from the convection, they also ended further to the south. Instead of just red trajectories (43N) originating in the east at higher levels AGL, like at 0000 UTC, at 0300 UTC there were also orange and yellow trajectories from the east (42N and 41N, respectively; Fig. 13(c-e)). These parcels also have the lowest CAPE (Fig. 10a-c). The remaining parcels coming from the westsouthwest at 1.0-2.0 km match the wind shift occuring at lower levels in figure 5. Also of note, figures 10e and 10f show the areas with highest CAPE come from parcels at 1.0 km. Those parcels at 1.0 km (corresponding to latitudes with blue stars or purple diamonds, 39N and 38N, respectively) have taken a path from the south of their ending location (Fig. 13c).

Back-trajectories ending at 0600 UTC follow the same pattern at low levels as at

0000 UTC and 0300 UTC with the majority of parcels originating from the east (IL, IN, IA; Figs. 14a-b). At higher altitude more parcels have traveled from the west-southwest (Figs. 14c-d). This also agrees with figure 6, where the wind shift occurs between 1.0 km and 1.5 km. The 2.0 km back-trajectories show the largest change in parcel travel within the 24 hours prior (Fig. 14e). Four trajectories maintain their eastward path (Fig. 14e) with all four of those parcels ending furthest from the convective line than any other parcel trajectory at the same latitude. Similar to what was seen in 0300 UTC, more parcels ending further to the south originated from the east than the previous time. At levels 1.0-2.0 km AGL, 0000 UTC parcels originating from the east only ended at 43N; at 0300 UTC parcels origniating from the east ended at 43N, 42N, and 41N; at 0600 UTC parcels originating from the east ended at 43N south to 40N. All seventeen remaining trajectories at 0600 UTC have originated from the west or northwest of their ending location with the majority originating in NE. Recalling figure 11f, there was a noticeable difference in CAPE at 1.0 km and 1.5 km compared to the other three levels and the other locations to the north of 38N. In figure 11f, 1.0 and 1.5 km would correspond to the purple diamond (38N) trajectories in figure 14c and d, respectively. The other levels with lower CAPE in figure 11f correspond to the purple diamond trajectories in figure 14a, b, and e. The parcels with the MU CAPE at 1.0 and 1.5 km (Fig. 11f) originated in KS, traveling mostly from the west of their ending location (Figs.14c-d). The parcels with less CAPE at the other three heights AGL (Fig. 11f) originated from OK and MO, taking a path from the south of their ending location (Figs. 14a-b), or they originated in NE, taking a path from the northwest of their ending location (Fig. 14e). This suggests that the parcels originating in the airmass to the west of the convection was able to sustain the MCS at 0600 UTC while parcels originating in the

airmass to the south, northwest, or east could not sustain elevated convection. With decreasing CAPE through the overnight hours and lack of support from a low-level jet, the structure of the MCS weakens although convection persists post-sunrise on 10 August (not shown) with the airmass with parcels originating from the west (purple diamonds) sustained convection the longest.

Chapter 6

Summary and Conclusions

On 9 August at approximately 2100 UTC, convection initiated in the lee of the Rocky Mountains. This convection grew upscale into a severe MCS traveling through the Great Plains during the overnight hours. Once the sun set, surface stabilization began, owing to radiational cooling as the pre-storm environment remained dry. CAPE at all levels decreased after sunset shifting the distribution of the most unstable CAPE from the surface to aloft. As the storm persisted, low-level mixing ceased, as evidenced by the stabilization of the boundary layer. This resulted in air parcels feeding the MCS to shift from surface-based to elevated. The elevated parcels were more unstable than the surface-based parcels but they also originated from a different air mass. While the system was surface-based, air parcels being ingested arrives at the convective line from the east and southeast (IL, IN, IA). As the system transitioned to elevated, the most unstable air parcels in the pre-storm environment arrived at the convective line from the west and southwest (NE, CO, NM). With a weak to non-existent low-level jet, this MCS was able to sustain itself after surface stabilizaton by tapping CAPE from elevated air parcels ahead of the line, but moving eastward aloft ahead of, and slower than the convective line.

The main findings from this study are:

1) The convective system was able to sustain convection from air parcels aloft with maximum MU CAPE in the absence of a low-level jet even after after the gust front surged far enough from the main convective line to no longer provide support for new initation. The air parcels providing the MU CAPE were from a different airmass compared to those when the surface was the source air for

convection.

2) The location AGL of MU CAPE transitioned from the surface to elevated during MCS evolution.
    a. CAPE at all heights AGL decreased as the surface stabilized.
    b. The surface was always the location of MU CAPE at 0000 UTC, before stablization and before sunset.
    c. Once the surface began to stabilize after sunset (0300 UTC), the location of MU CAPE varied along the convective line.
    d. After surface stabilization (0600 UTC), MU CAPE was always located above the surface. At the majority of locations it was located at 1.0 km.
3) Parcels along the convective line (at the same height) varied substantially along the line, specifically between 1.0 and 2.0 km.
    a. Starting at the north end of the convective line (43N), parcels are found orginating from the east.
    b. The middle section of the convective line (~42N-39N, depending on the time of evolution) parcels originated from all directions including northwest, west, southwest, and south of their ending locations.
    c. Parcels ending at 38N and 37N originated from the southeast, south, or southwest of their ending location.
4) Parcels along and ahead of the convective line originated in different airmasses depending on their height AGL.
    a. The majority of parcels ending at the surface and 500 m originated from the east or southeast of their ending locations at all three times.

b. At 1.0 and 1.5 km, parcels originated to the southeast of their ending location at 0000 UTC, they originated from the south at 0300 UTC, and from the southwest and west at 0600 UTC.

c. At 2.0 km parcels originated from the southwest and west at 0000 UTC and 0300 UTC and originated from the northwest of their ending location at 0600 UTC.

5) Parcels feeding the convective system originated in different airmasses depending on the point of MCS evolution.

a. Parcels originating from the east were the most unstable at 0000 UTC and resided at the surface.

b. Most unstable parcels at 0300 UTC resided at different heights along the line with the highest values of CAPE along the line associated with parcels originating south of their ending location.

c. CAPE at all points and levels weakened at 0600 UTC except in parcels originating from the west of their ending location. These parcels were feeding the portion of the MCS that was strongest, based on reflectivity.

Although this analysis is applicable to the MCS that occurred on 9 and 10 August 2014, further studies of the transition from surface-based convection to nocturnal, elevated MCS are needed to discern whether or not these results are unique to this case, or are applicable to the numerous similar events observed each year across the Great Plains.

Table

WRS-88D Locations Used for Analysis				
Time	**Grid Center**		**Radars Used Per Period**	
	Lat	**Lon**	**Radar Site**	**Radar Location**
20Z-00:55 UTC	39 N	103 W	KCYS	Cheyenne, WY
			KFTG	Denver, Co
			KGLD	Goodland, KS
			KPUX	Pueblo, CO
01Z-04:30 UTC	39 N	100 W	KDDC	Dodge City, KS
			KGLD	Goodland, KS
			KUEX	Hastings, NE
			KTWX	Topeka, KS
			KICT	Witchita, KS
04:35Z-06:00 UTC	39 N	98 W	KDDC	Dodge City, KS
			KGLD	Goodland, KS
			KUEX	Hastings, NE
			KTWX	Topeka, KS
			KICT	Witchita, KS

Table 1: Columns Right to left- 1) times where compositing was done on the same grid; 2) latitudes and longitudes of the center of each grid that 88D reflectivity was composited; 3) 88D identifier for radars used in the composite; 4) Location of 88D radar site.

Figures

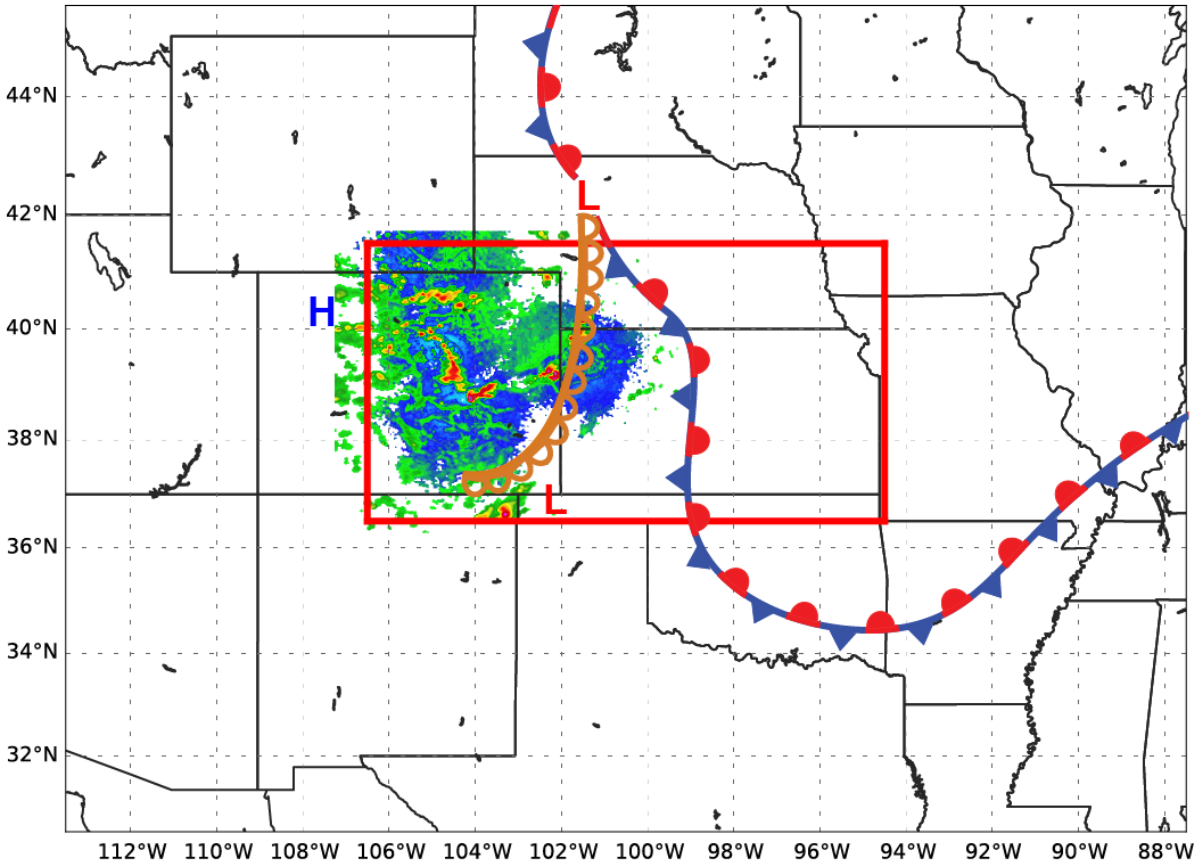

Figure 1: Surface analysis of pressure systems and fronts is plotted from data at 2100 UTC 9 August 2014. Thick red box is the analysis domain during the MCS lifetime. Reflectivity is plotted from WSR-88D data at 2100 UTC 9 August 2014.

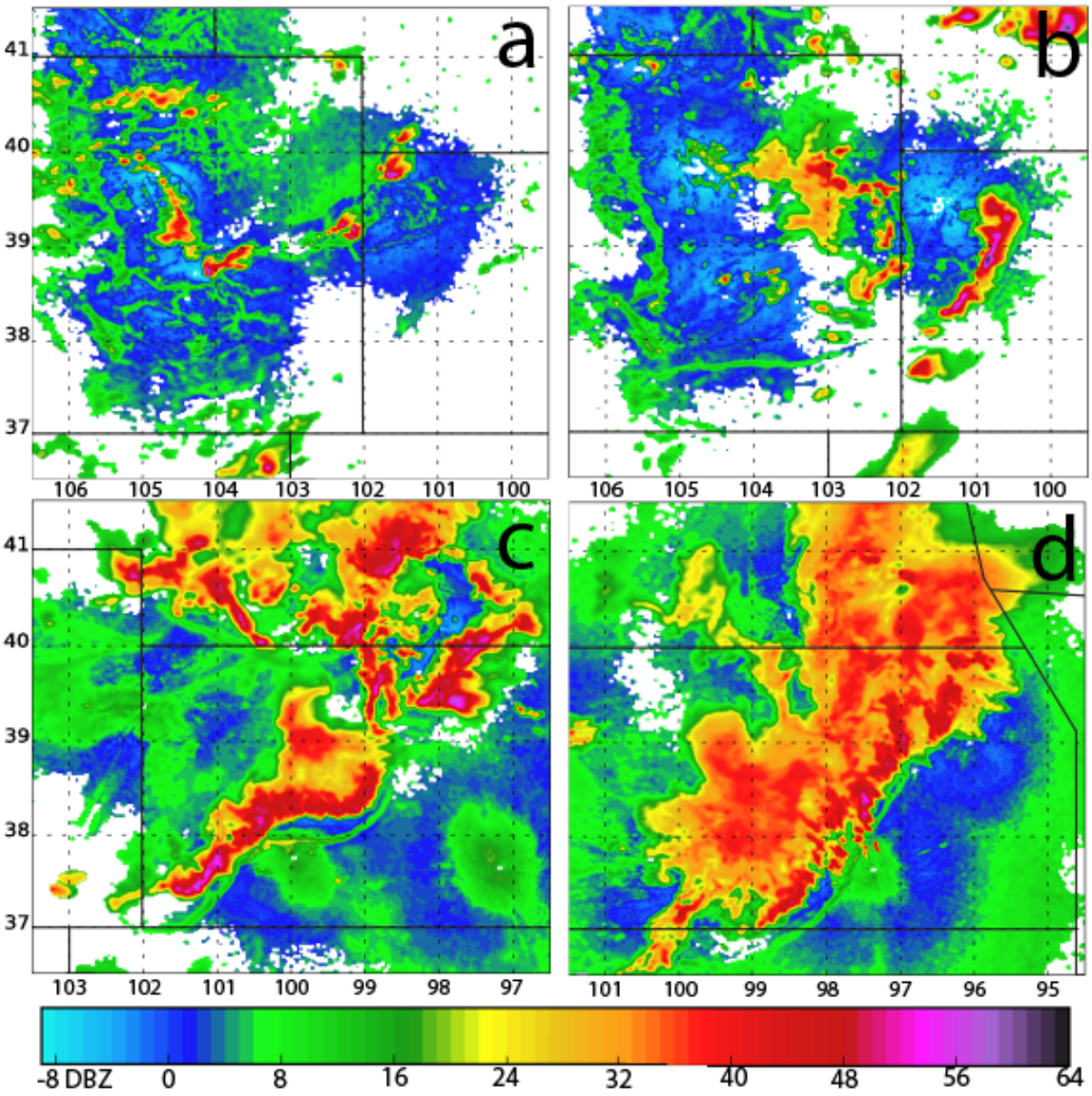

Figure 2: Observed WSR-88D reflectivity composites every three hours at 2100 UTC (a), 0000 UTC (b), 0300 UCT (c), and 0600 UTC (d). Note the domain shift from (b) to (c) and from (c) to (d).

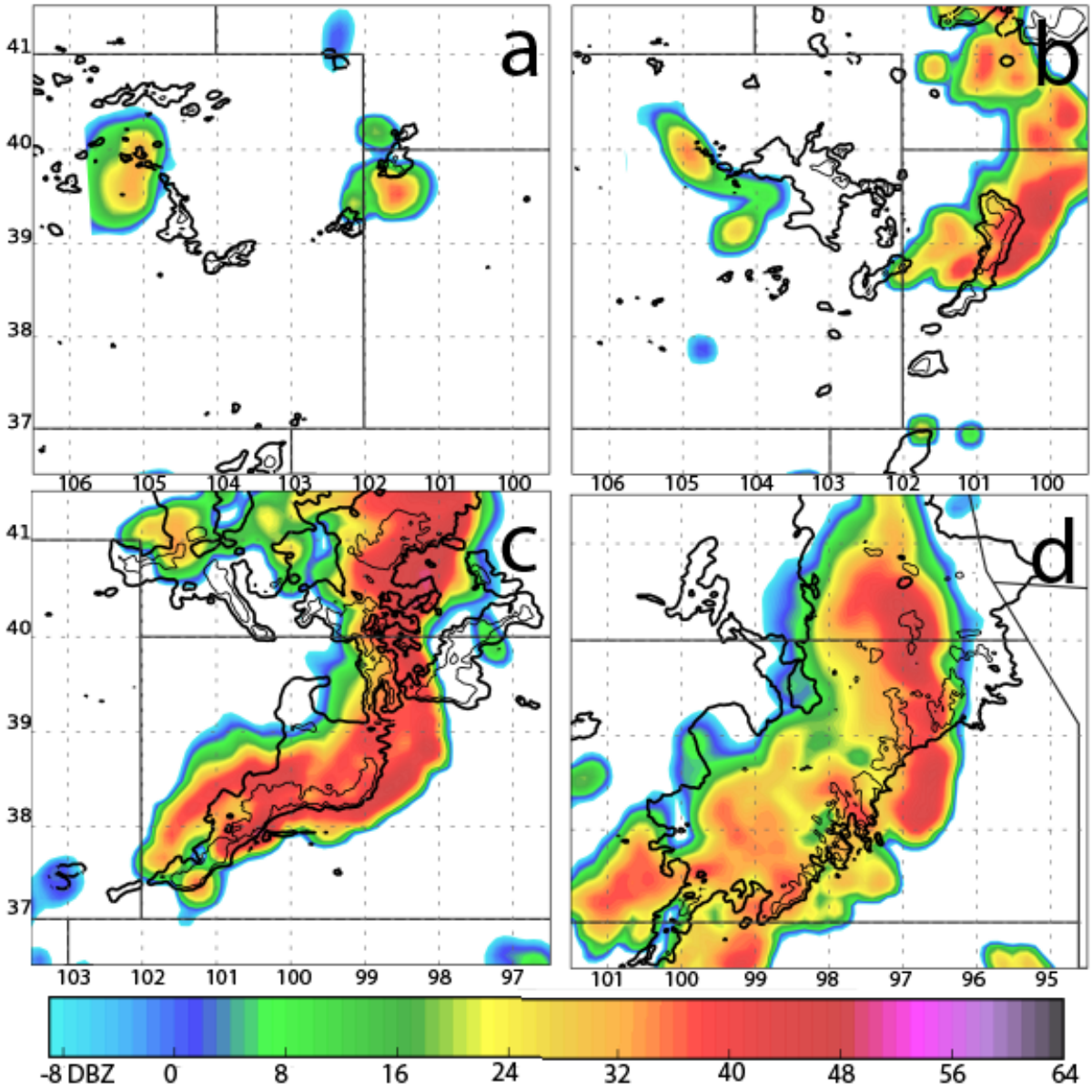

Figure 3: Simulated WRF reflectivity contoured every three hours at 2100 UTC (a), 0000 UTC (b), 0300 UTC (c), and 0600 UTC (d), times corresponding to the data on Fig. 2. The thick black contour in each frame is observed 20 dBZ reflectivity and the thin black contour is observed 40 dBZ reflectivity at the same time as simulated reflectivity. Note the domain shift from (b) to (c) and from (c) to (d).

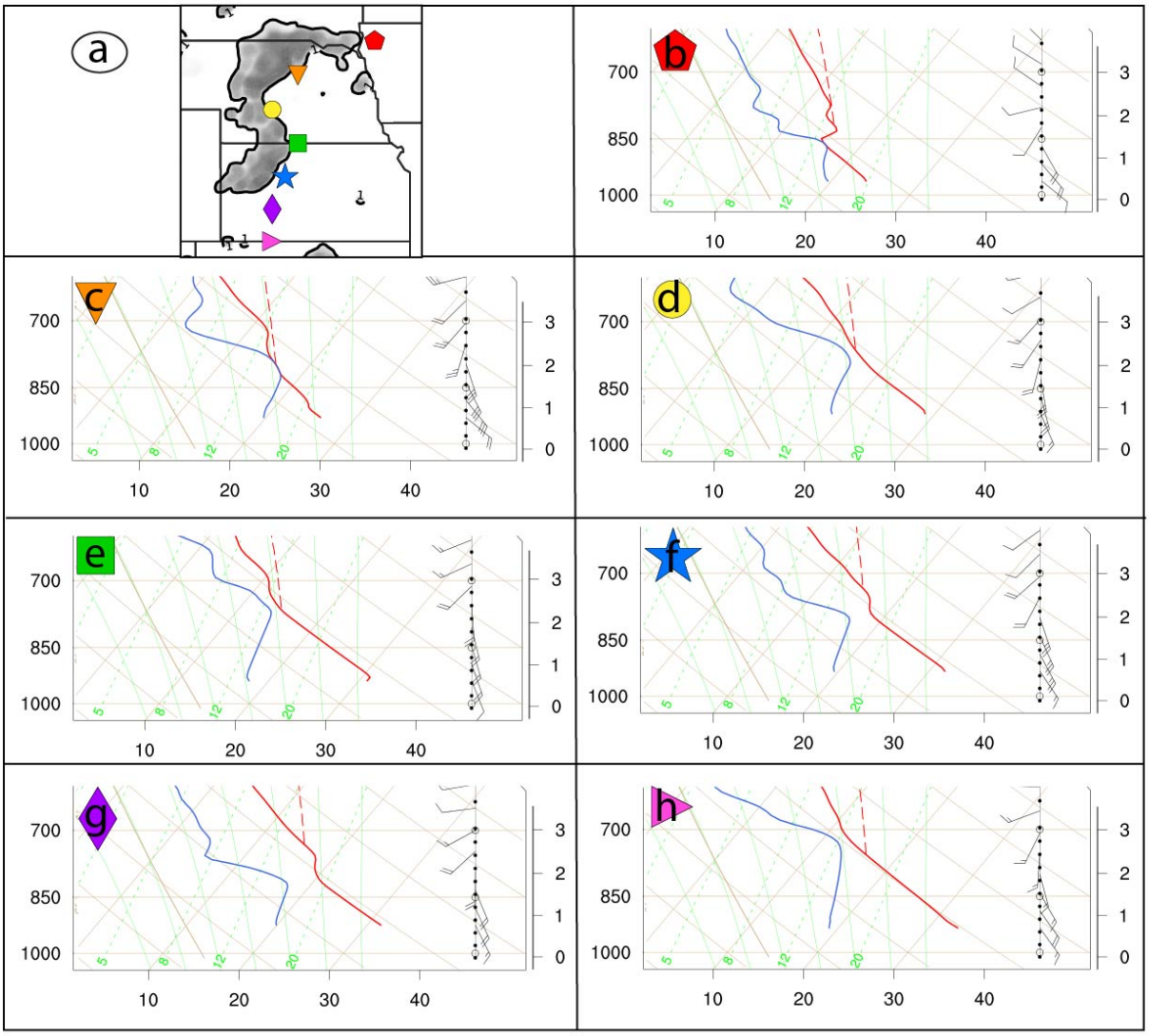

Figure 4: (a) WRF reflectivity at 0000 UTC with the symbols representing the location of the model soundings in (b-h). (b-h): the lowest 4.0 km of WRF model soundings at the location of the symbols on Figure 4a. The red line is temperature and the blue line dew point temperature. Temperature is in Celsius. Red dashed lines represent parcel pseudo-adiabatic ascent above the level of free convection for parcels originating at the surface. The left axis is pressure in millibars, while the right axis is height in kilometers.

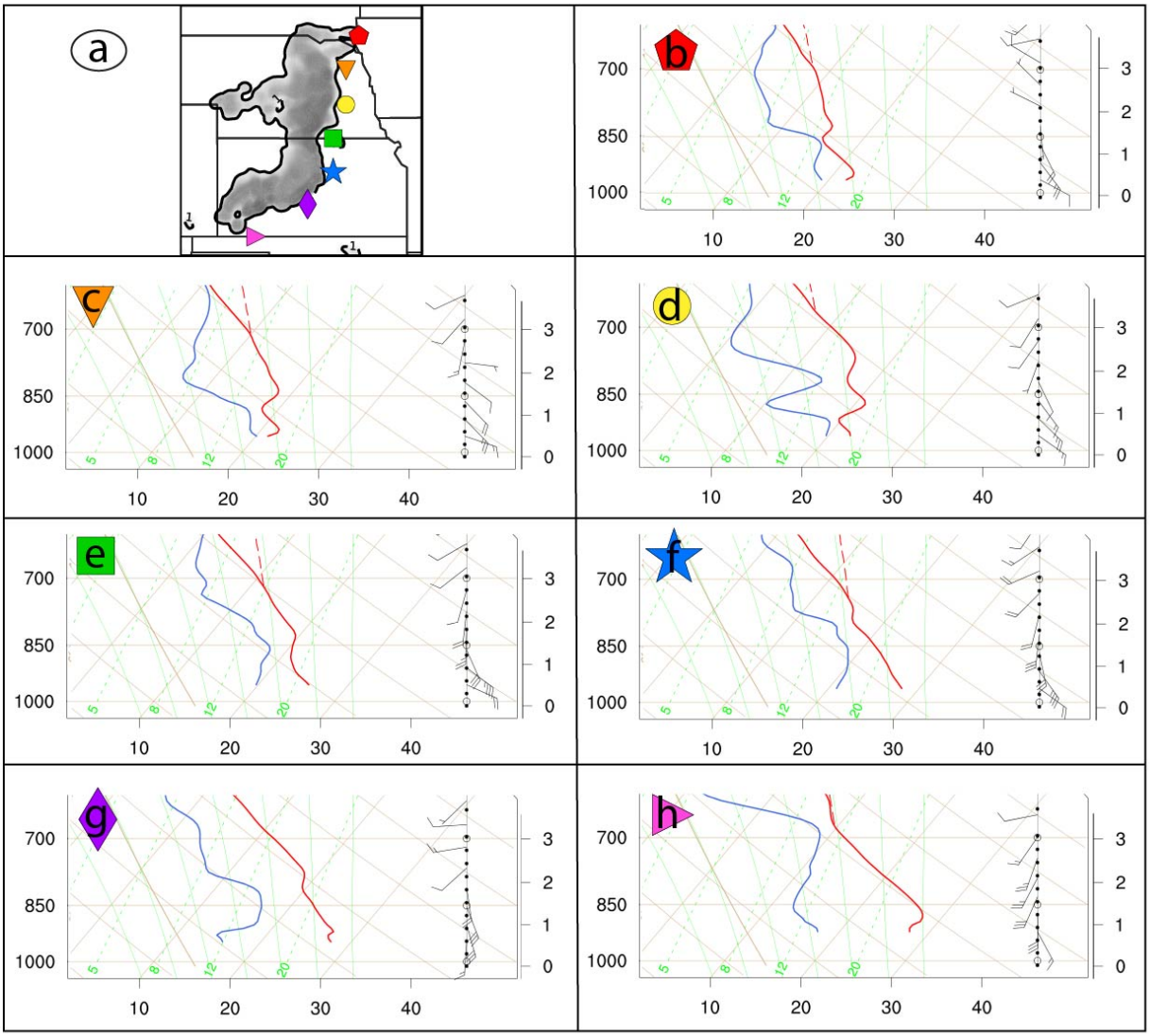

Figure 5: As in Fig. 4 but at 0300 UTC.

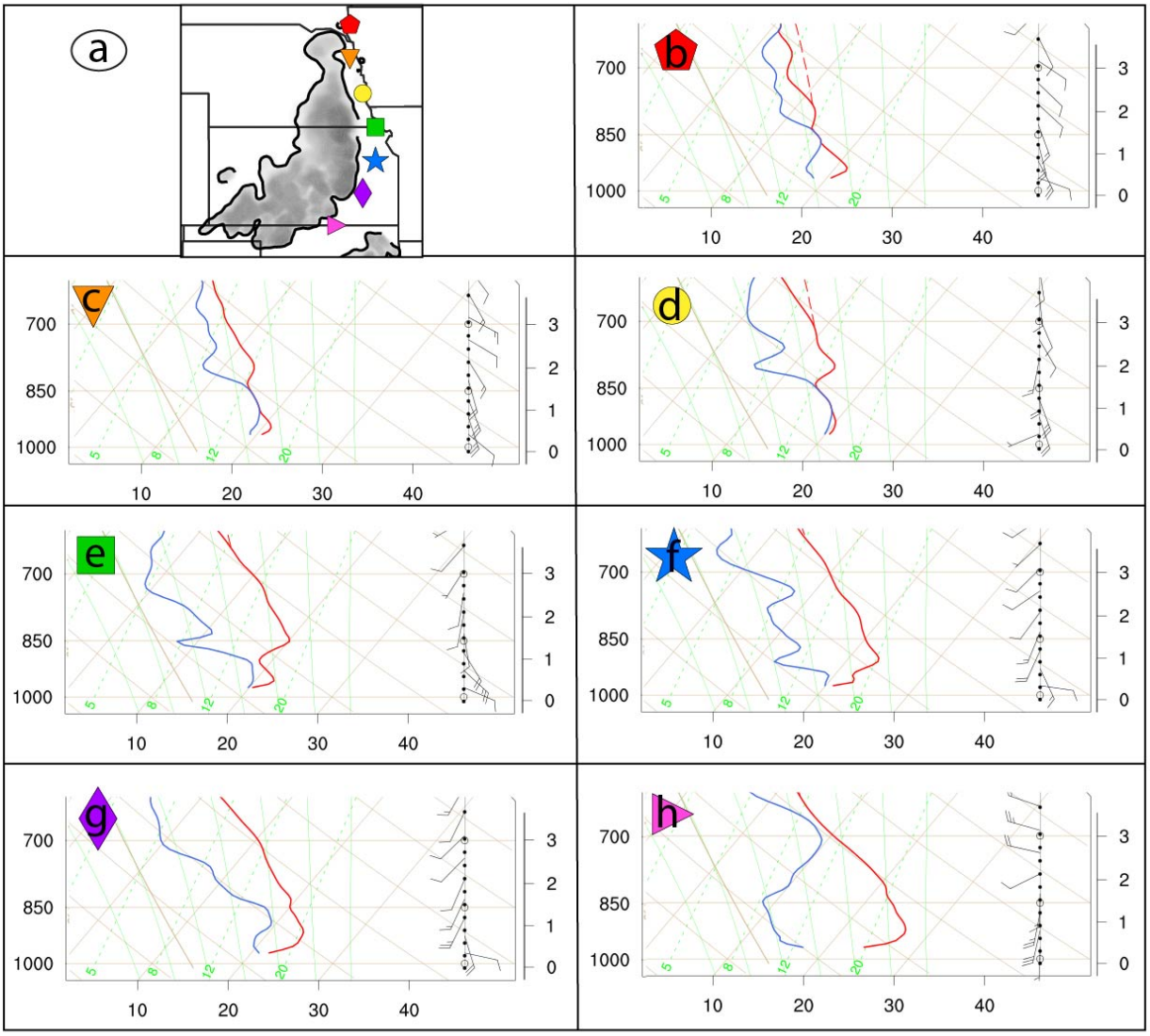

Figure 6: As in Fig. 4 but at 0600 UTC.

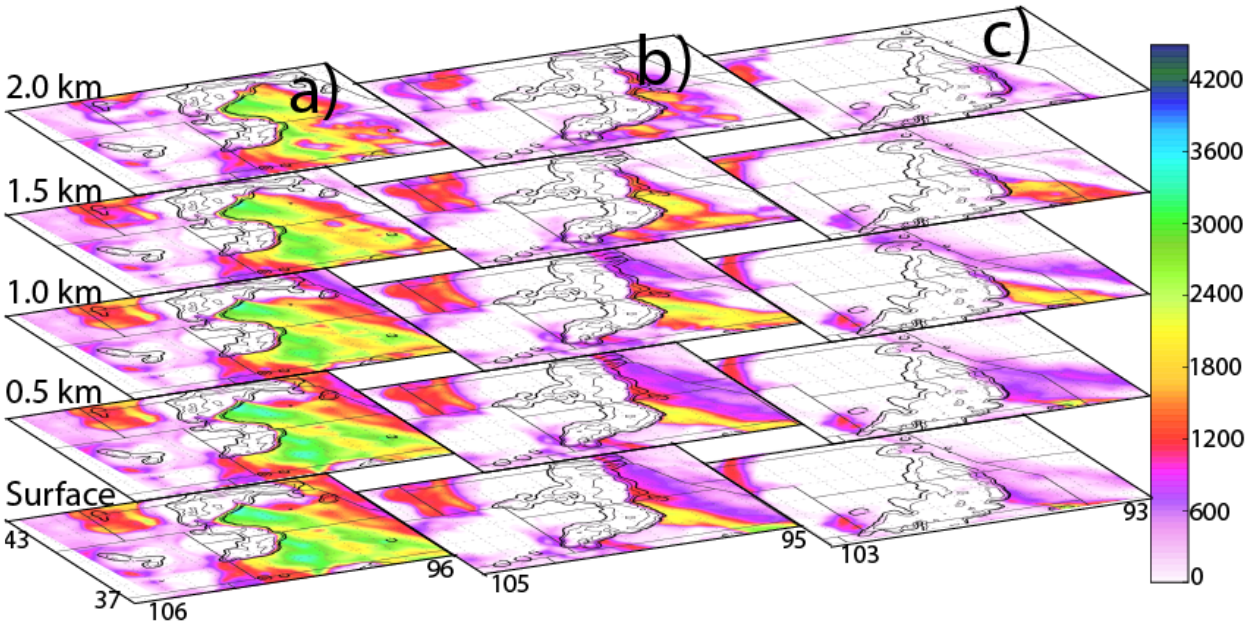

Figure 7: CAPE color contoured for parcels originating at five levels and three times. Columns go from the surface to 2.0 km above ground level (AGL). The thick black contour is 1 dBZ WRF reflectivity and the thin contours are 20 dBZ and 40 dBZ, respectively. Column a) is at 0000 UTC. Column b) is at 0300 UTC. Column c) is at 0600 UTC.

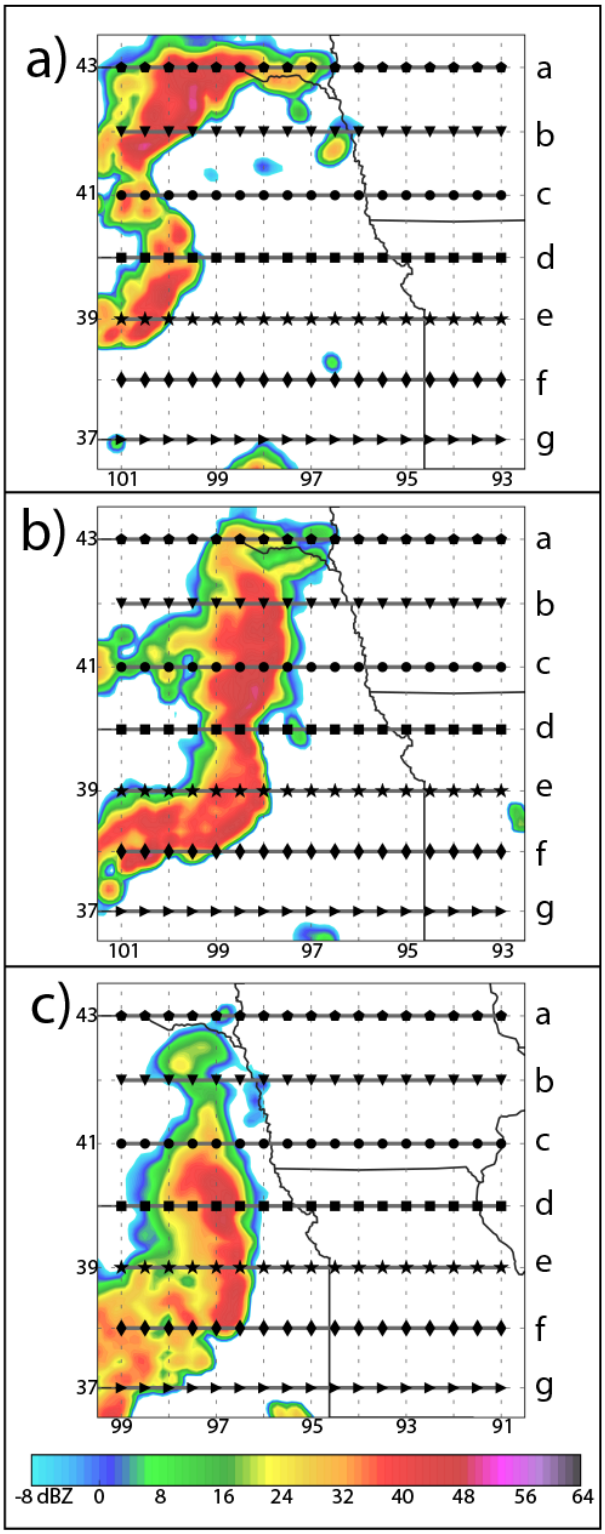

Figure 8: Black points on Fig. 8 a-c show the locations where CAPE was calculated at different levels relative to the MCS. CAPE values are displayed in Figs. 9-11 (a-g). Letters on the right y-axis correspond to panels a-g in Figs. 9-11. Fig. 8a is at 0000 UTC. Fig. 8b is at 0300 UTC. Fig. 8c is at 0600 UTC.

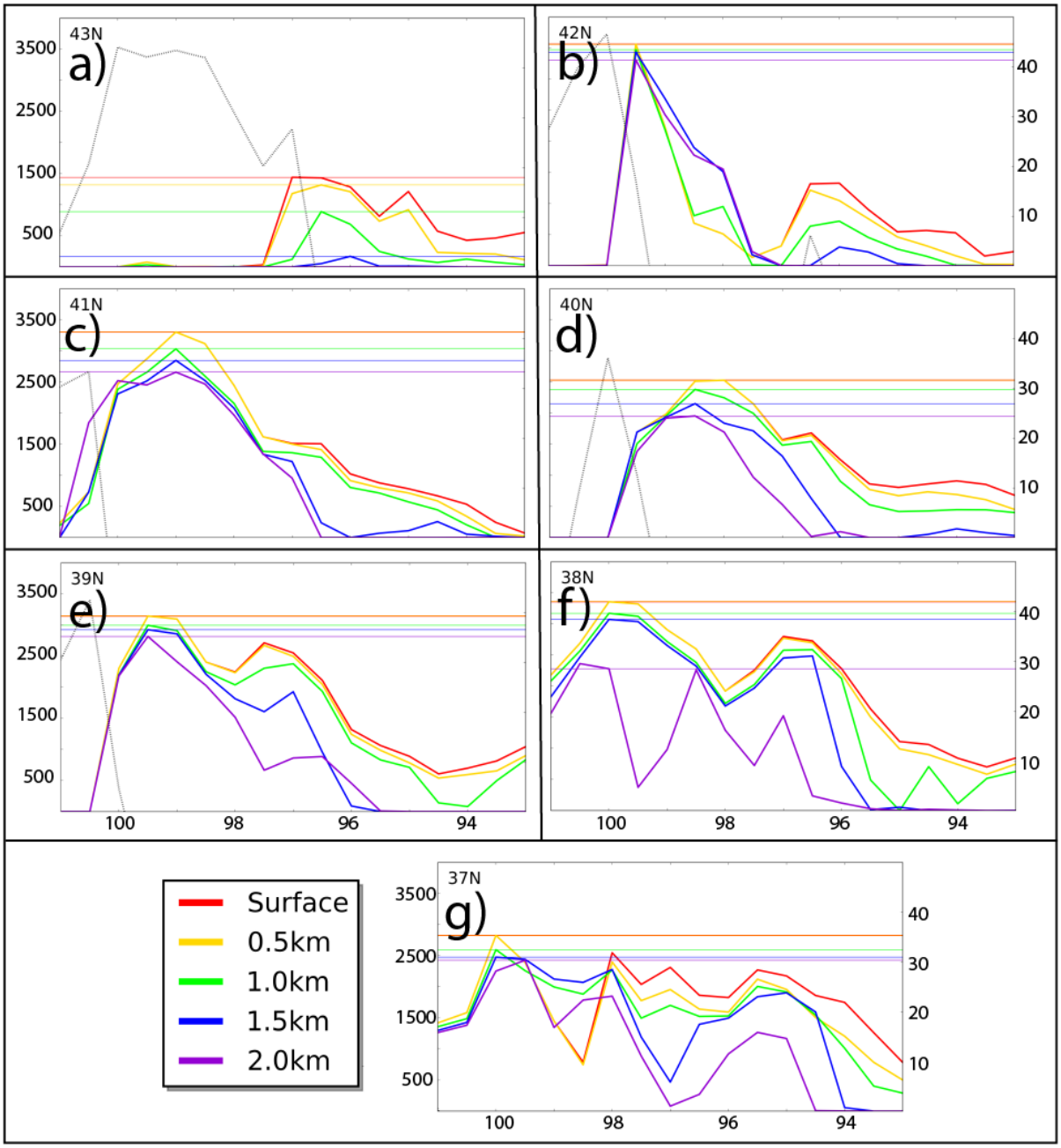

Figure 9: Figs. 9 (a-g) show CAPE and reflectivity at each point across the domain in Fig. 8a. Gray dotted lines are reflectivity. Reflectivity scale is on the right y-axis. Colored lines show CAPE at each level according to the legend located to the left of Fig. 9g. The CAPE scale is on the left y-axis. Horizontal colored lines show the maximum CAPE value of each level.

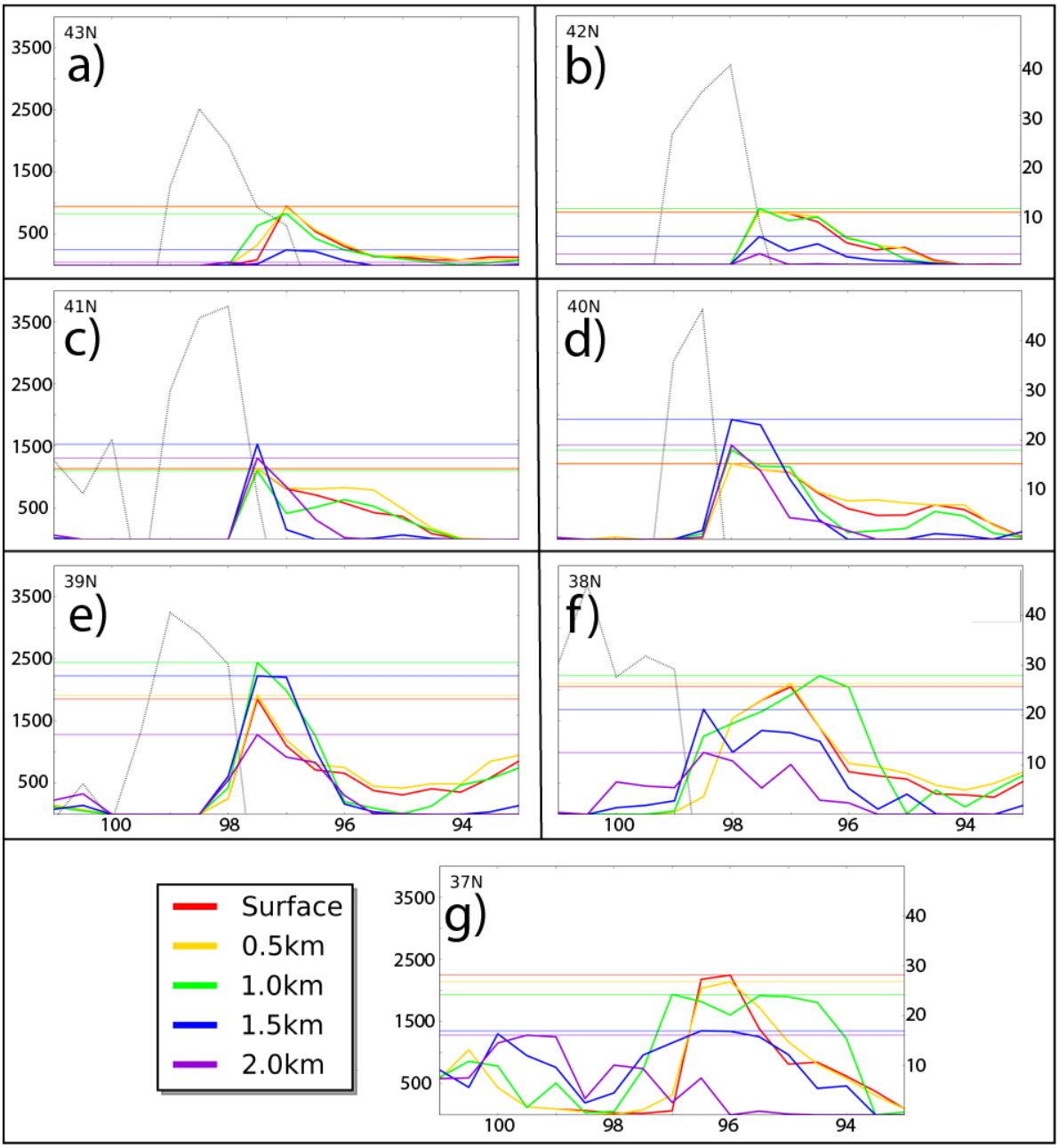

Figure 10: All figures as in Figure 9 but at 0300 UTC.

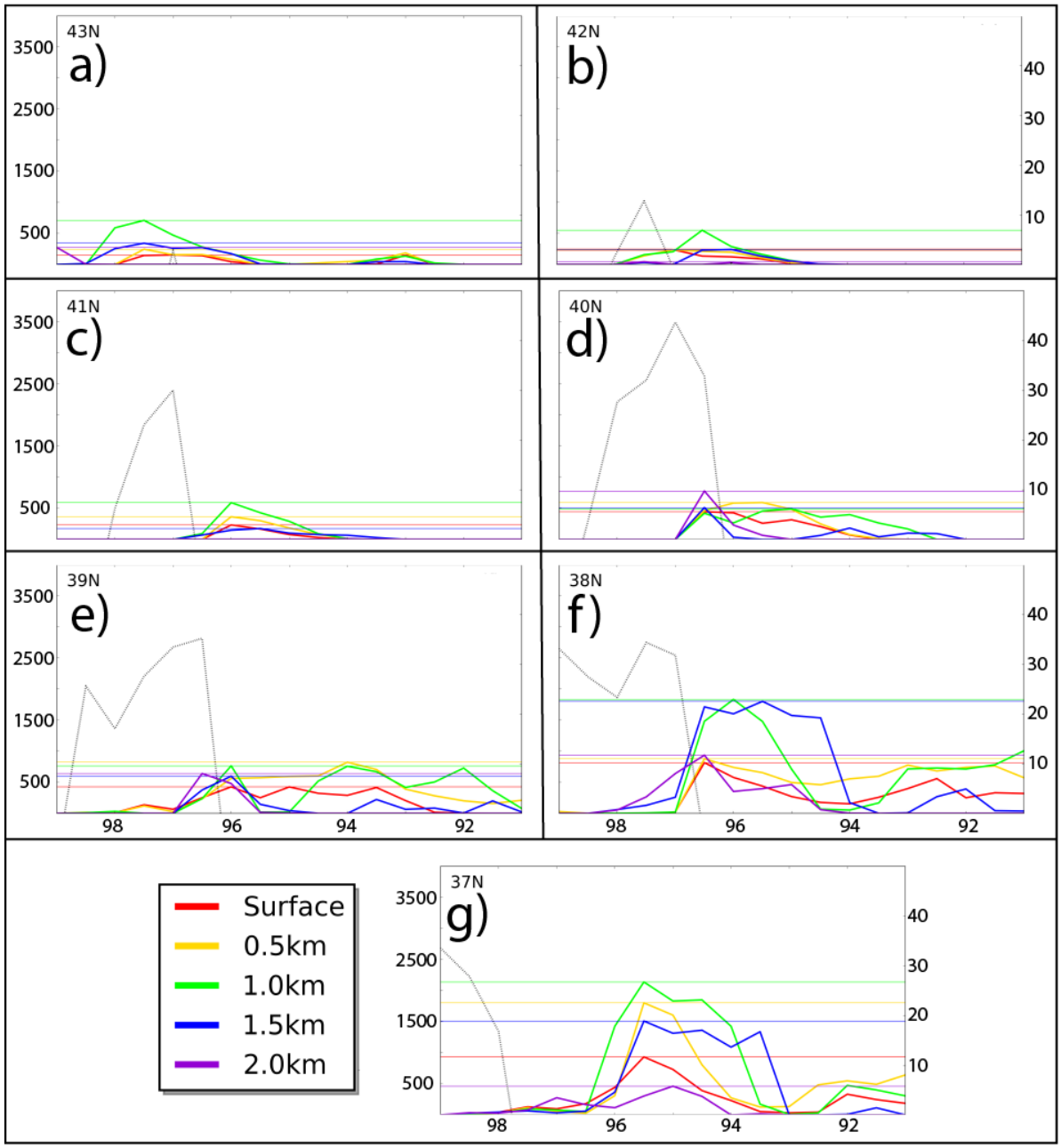

Figure 11: All figures follow the same description as Figure 9 but at 0600 UTC.

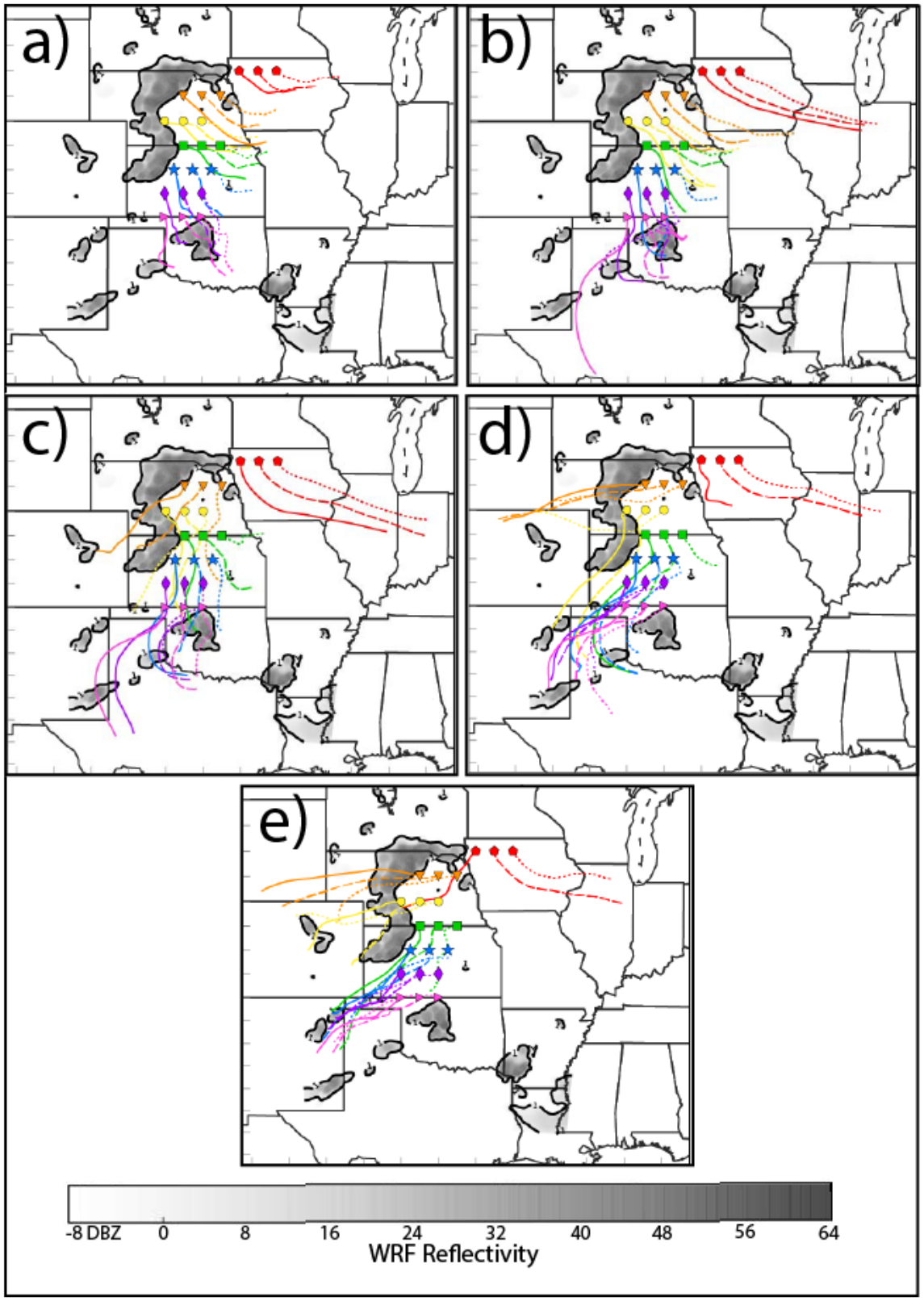

Figure 12: Symbols in each panel denote the ending point of the back-trajectory. The opposite end of the line is where the parcel was located 24 hours prior. In these

images, the symbols are the locations of the parcels at 0000 UTC 10 August 2014. The opposite end of each trajectory is the location of the parcel at 0000 UTC 9 August 2014. Solid lines are the trajectories closest to the convective line. Dashed and dotted lines end one and two longitudinal points (111km and 222 km, respectively) away from the solid line's end point, respectively. Figure 12a represents trajectories ending at the surface. Trajectories in 12b, 12c, 12d, and 12e end at 500 m, 1.0 km, 1.5 km, and 2.0 km, respectively. WRF reflectivity at 0000 UTC is plotted under the trajectories.

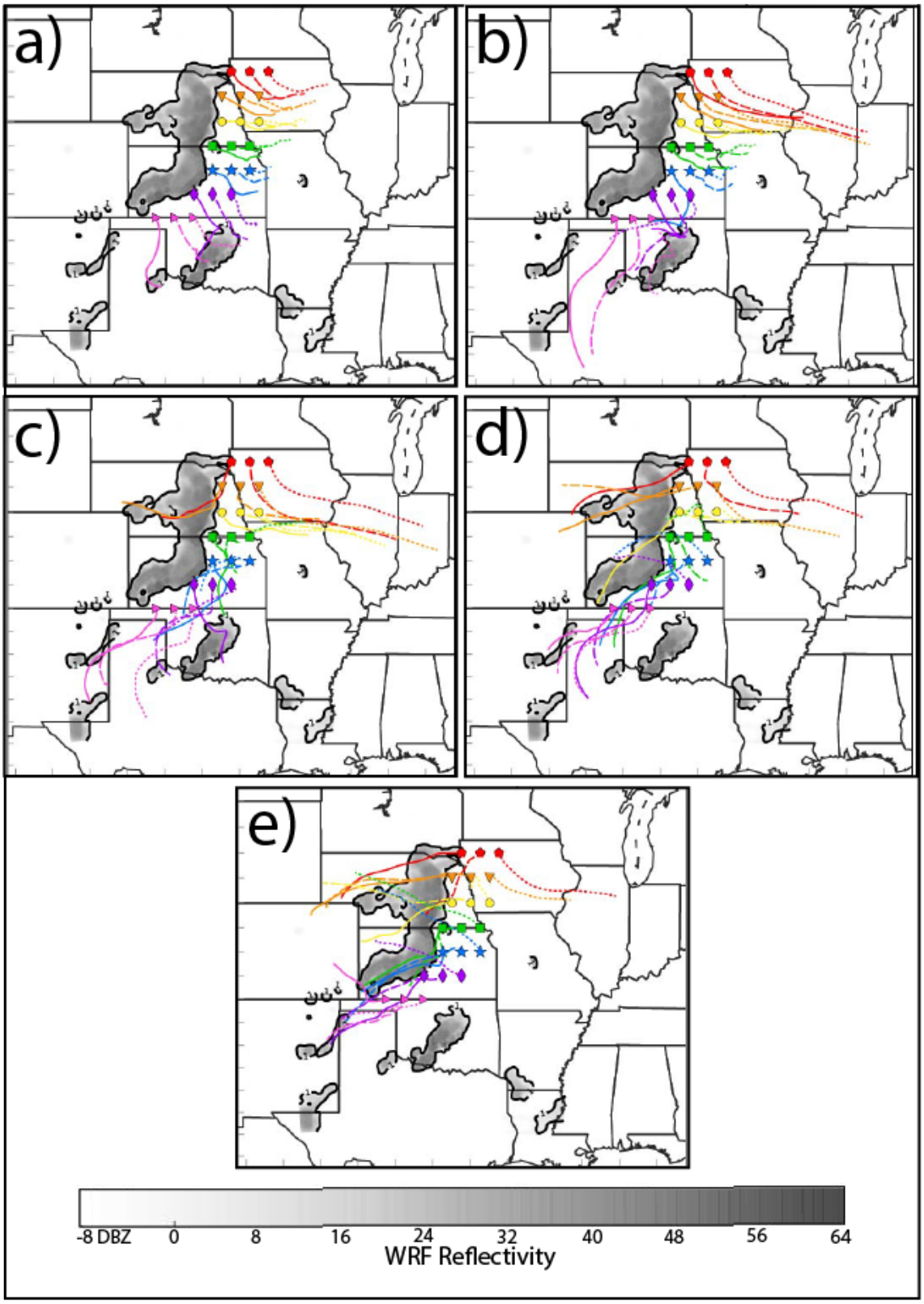

Figure 13: Figure 13(a-e) same as Figure 12 but with back-trajectories released at 0300 UTC.

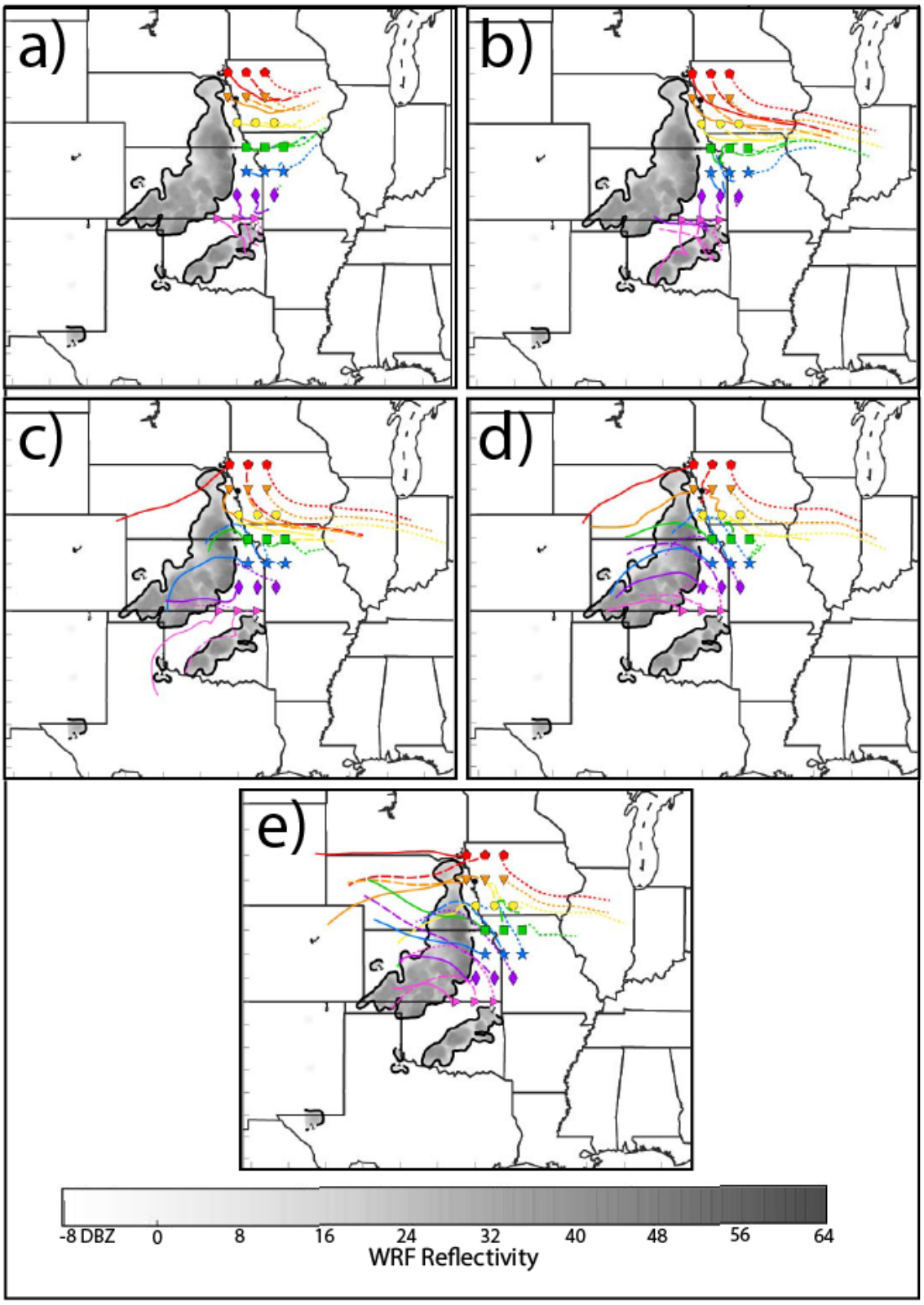

Figure 14: Figure 14(a-e) same as Figure 12 but with back-trajectories released at 0600 UTC.

References

Atkins, NT, and JJ Cunningham, 2006: 6.4 THE INFLUENCE OF LOW-LEVEL STABLE LAYERS ON DAMAGING SURFACE WINDS WITHIN BOW ECHOES. https://ams.confex.com/ams/pdfpapers/115292.pdf.

Alam, K, S Qureshi, and T Blaschke, 2011: Monitoring spatio-temporal aerosol patterns over Pakistan based on MODIS, TOMS and MISR satellite data and a HYSPLIT model. *Atmospheric Environment*,. http://www.sciencedirect.com/science/article/pii/S1352231011005619.

American Meteorological Society, cited 2016: "elevated convection". Glossary of Meteorology. [Available online at http://glossary.ametsoc.org/wiki/"elevated convection"]

Billings, J., and M. Parker, 2012: Evolution and Maintenance of the 22–23 June 2003 Nocturnal Convection during BAMEX. *Weather Forecast*, **27**, 279–300, doi:10.1175/WAF-D-11-00056.1.

Blanchard, D. O., 1998: Assessing the vertical distribution of convective available potential energy. *Wea. Forecasting*, **13,** 870877.

Bradley, A. A., and J. A. Smith, 1994: The hydrometeorological environment of extreme rainstorms in the southern plains of the United States. *Journal of Applied Meteorology*, **33**, 1418–1431. http://journals.ametsoc.org/doi/abs/10.1175/1520-0450(1994)033%3C1418:THEOER%3E2.0.CO%3B2.

Bryan, GH, 2005: Spurious convective organization in simulated squall lines owing to moist absolutely unstable layers. *Monthly weather review*,. http://journals.ametsoc.org/doi/abs/10.1175/MWR2952.1.

Bryan, GH, and ML Weisman, 2006: MECHANISMS FOR THE PRODUCTION OF SEVERE SURFACE WINDS 7.5 IN A SIMULATION OF AN ELEVATED CONVECTIVE SYSTEM. http://www2.mmm.ucar.edu/people/bryan/Papers/bryan_weisman_2006_SLS.pdf.

Colman, BR, 1990a: Thunderstorms above frontal surfaces in environments without positive CAPE. Part I: A climatology. *Monthly weather review*,. http://journals.ametsoc.org/doi/abs/10.1175/1520-0493(1990)118%3C1103:TAFSIE%3E2.0.CO;2.

Colman, BR, 1990b: Thunderstorms above frontal surfaces in environments without positive CAPE. Part II: Organization and instability mechanisms. *Monthly weather review*,. http://journals.ametsoc.org/doi/abs/10.1175/1520-0493(1990)118%3C1123:TAFSIE%3E2.0.CO%3B2.

Dreher, JG, 2009: Configuring the HYSPLIT model for national weather service forecast office and spaceflight meteorology group applications. http://ntrs.nasa.gov/search.jsp?R=20090023414.

Du, Y., and R. Rotunno, 2014: A Simple Analytical Model of the Nocturnal Low-Level Jet over the Great Plains of the United States. *J Atmos Sci*, **71**, 3674–3683, doi:10.1175/JAS-D-14-0060.1.

Erlingis, JM, and AP Barros, 2014: A study of the role of daytime land–atmosphere interactions on nocturnal convective activity in the southern Great Plains during CLASIC. *Journal of Hydrometeorology*,. http://journals.ametsoc.org/doi/abs/10.1175/JHM-D-14-0016.1.

French, A., and M. Parker, 2010: The Response of Simulated Nocturnal Convective Systems to a Developing Low-Level Jet. *J Atmos Sci*, **67**, 3384–3408,

doi:10.1175/2010JAS3329.1.

Fritsch, JM, RJ Kane, and CR Chelius, 1986: The contribution of mesoscale convective weather systems to the warm-season precipitation in the United States. *Journal of climate and ...*,. http://journals.ametsoc.org/doi/abs/10.1175/1520-0450(1986)025%3C1333:TCOMCW%3E2.0.CO;2.

Han, YJ, TM Holsen, and PK Hopke, 2005: Comparison between back-trajectory based modeling and Lagrangian backward dispersion modeling for locating sources of reactive gaseous mercury. *Environmental science & ...*, doi:10.1021/es0498540. http://pubs.acs.org/doi/abs/10.1021/es0498540.

Horgan, K., D. Schultz, J. Hales, S. Corfidi, and R. Johns, 2007: A Five-Year Climatology of Elevated Severe Convective Storms in the United States East of the Rocky Mountains. *Weather Forecast*, **22**, 1031–1044, doi:10.1175/WAF1032.1.

Houze, R., 2004: Mesoscale convective systems. *Rev Geophys*, **42**, doi:10.1029/2004RG000150.

Iacono, M., J. S. Delamere, E. J. Mlawer, M. W. Shephard, S. A. Clough, and W. D. Collins, 2008: Radiative forcing by long-lived greenhouse gases: Calculations with the AER radiative transfer models. *J. Geophys. Res.-Atmos.*, **113**(D13), D13103, doi:10.1029/2008JD009944.

Doswell,C.A., III, and E. N. Rasmussen, 1994: The effect of neglecting the virtual temperature correction on CAPE calculations. *Weather and forecasting*, **9**, 625–629. http://journals.ametsoc.org/doi/abs/10.1175/1520-0434(1994)009%3C0625:TEONTV%3E2.0.CO;2.

James, R., and P. Markowski, 2010: A Numerical Investigation of the Effects of Dry Air Aloft

on Deep Convection. *Mon Weather Rev*, **138**, 140–161, doi:10.1175/2009MWR3018.1.

Janjic, ZI, 1994: The step-mountain eta coordinate model: Further developments of the convection, viscous sublayer, and turbulence closure schemes. *Monthly Weather Review*, doi:10.1175/1520-0493(1994)122<0927:TSMECM>2.0.CO;2. http://journals.ametsoc.org/doi/abs/10.1175/1520-0493(1994)122%3C0927:TSMECM%3E2.0.CO%3B2.

Kincer, JB, 1916: Daytime and nighttime precipitation and their economic significance. *Monthly Weather Review*,. http://journals.ametsoc.org/doi/abs/10.1175/1520-0493(1916)44%3C628:DANPAT%3E2.0.CO%3B2.

McCaul, E. W., and M. L. Weisman, 1996: Simulations of shallow supercells in landfalling hurricane environments. *Mon. Wea. Rev*., **124,** 408-429

McGowan, H, and A Clark, 2008: Identification of dust transport pathways from Lake Eyre, Australia using Hysplit. *Atmospheric Environment*,. http://www.sciencedirect.com/science/article/pii/S1352231008004950.

Moore, J., F. Glass, C. Graves, S. Rochette, and M. Singer, 2003: The Environment of Warm-Season Elevated Thunderstorms Associated with Heavy Rainfall over the Central United States. *Weather Forecast*, **18**, 861–878, doi:10.1175/1520-0434(2003)018<0861:TEOWET>2.0.CO;2.

Rauber, R. M., M. K. Macomber, D. M. Plummer, A. A. Rosenow, G. M. McFarquhar, B. F. Jewett, D. Leon, and J. M. Keeler, 2014: Finescale Radar and Airmass Structure of the Comma Head of a Continental Winter Cyclone: The Role of Three Airstreams. *Mon. Wea. Rev*., 142, 4207-4229

Rauber, R. M., D. M. Plummer, M. K. Macomber, A. A. Rosenow, G. M. McFarquhar, B. F. Jewett, D. Leon, Nathan Owens and J. M. Keeler, 2015: The role of generating cells and boundary-layer circulations in the fine-scale structure of a winter cyclone over the Great Lakes. Mon. Wea. Rev., 143, 2291-2318.

Rochette, SM, and JT Moore, 1996: Initiation of an elevated mesoscale convective system associated with heavy rainfall. *Weather and forecasting*,. http://digitalcommons.brockport.edu/esc_facpub/5/.

Schmidt, JM, and WR Cotton, 1989: A high plains squall line associated with severe surface winds. *Journal of the Atmospheric Sciences*,. http://journals.ametsoc.org/doi/abs/10.1175/1520-0469(1989)046%3C0281:AHPSLA%3E2.0.CO%3B2.

Schumacher, RS, and RH Johnson, 2005: Organization and environmental properties of extreme-rain-producing mesoscale convective systems. *Monthly weather review*,. http://journals.ametsoc.org/doi/abs/10.1175/MWR2899.1.

Schumacher, RS, and RH Johnson, 2006: Characteristics of US extreme rain events during 1999-2003. *Weather and Forecasting*,. http://journals.ametsoc.org/doi/abs/10.1175/WAF900.1.

Schumacher, R., 2015: Sensitivity of Precipitation Accumulation in Elevated Convective Systems to Small Changes in Low-Level Moisture. *J Atmos Sci*, **72**, 2507–2524, doi:10.1175/JAS-D-14-0389.1.

Stein, AF, RR Draxler, and GD Rolph, 2015: NOAA's HYSPLIT atmospheric transport and dispersion modeling system. *Bulletin of the ...*,. http://journals.ametsoc.org/doi/abs/10.1175/BAMS-D-14-00110.1.

Stevenson, S., and R. Schumacher, 2014: A 10-Year Survey of Extreme Rainfall Events in the Central and Eastern United States Using Gridded Multisensor Precipitation Analyses. *Mon Weather Rev*, **142**, 3147–3162, doi:10.1175/MWR-D-13-00345.1.

Thompson, G., P.R. Field, R.M. Rasmussen, and W.D. Hall, 2008: Explicit forecasts of winter precipitation using an improved bulk microphysics scheme. Part II: Implementation of a new snow parameterization. *Mon. Wea. Rev*., **12**, 5095-5115.

Trapp, R., S. Tessendorf, E. Godfrey, and H. Brooks, 2005: Tornadoes from Squall Lines and Bow Echoes. Part I: Climatological Distribution. *Weather Forecast*, **20**, 23–34, doi:10.1175/WAF-835.1.

Trier, S., C. Davis, D. Ahijevych, M. Weisman, and G. Bryan, 2006: Mechanisms Supporting Long-Lived Episodes of Propagating Nocturnal Convection within a 7-Day WRF Model Simulation. *J Atmos Sci*, **63**, 2437–2461, doi:10.1175/JAS3768.1.

Trier, S., C. Davis, D. Ahijevych, and K. Manning, 2014: Use of the Parcel Buoyancy Minimum (Bmin) to Diagnose Simulated Thermodynamic Destabilization. Part II: Composite Analysis of Mature MCS Environments. *Mon Weather Rev*, **142**, 967–990, doi:10.1175/MWR-D-13-00273.1.

Wakimoto, RM, HV Murphey, and A Nester, 2006: High winds generated by bow echoes. Part I: Overview of the Omaha bow echo 5 July 2003 storm during BAMEX. *Monthly weather ...*,. http://journals.ametsoc.org/doi/abs/10.1175/MWR3215.1.

Wallace, JM, 1975: Diurnal variations in precipitation and thunderstorm frequency over the conterminous United States. *Monthly Weather Review*,. http://journals.ametsoc.org/doi/abs/10.1175/1520-0493(1975)103%3C0406:DVIPAT%3E2.0.CO;2.

Weisman, ML, 1993: The genesis of severe, long-lived bow echoes. *Journal of the atmospheric sciences*,. http://journals.ametsoc.org/doi/abs/10.1175/1520-0469(1993)050%3C0645:TGOSLL%3E2.0.CO%3B2.

Wu, CM, B Stevens, and A Arakawa, 2009: What controls the transition from shallow to deep convection? *Journal of the Atmospheric …*,. http://journals.ametsoc.org/doi/abs/10.1175/2008JAS2945.1.

Yerramilli, A, V. Dodla, VS Challa, and LT Myles, 2012: An integrated WRF/HYSPLIT modeling approach for the assessment of PM2. 5 source regions over the Mississippi Gulf Coast region. *Air Quality*,. http://link.springer.com/article/10.1007/s11869-010-0132-1.